

Kinematics of Lagrangian Flow Separation in External Aerodynamics

Bjoern F. Klose* and Gustaaf B. Jacobs†

San Diego State University, San Diego, California 92182

and

Mattia Serra‡

Harvard University, Cambridge, Massachusetts 02138

<https://doi.org/10.2514/1.J059026>

Kinematic aspects of flow separation in external aerodynamics are investigated in the Lagrangian frame. Specifically, the initial motion of upwelling fluid material from the wall is related to the long-term attracting manifolds in the flowfield. Although the short-time kinematics are governed by the formation of a material spike upstream of the zero-skin-friction point and ejection of particles in the direction of the asymptotic separation line, the trajectories of the fluid tracers are guided by attracting ridges in the finite-time Lyapunov exponents once they leave the vicinity of the wall. The wall signature of this initial fluid upwelling event, which is the so-called spiking point (Serra, M., Vetel, J., and Haller, G., “Exact Theory of Material Spike Formation in Flow Separation,” *Journal of Fluid Mechanics*, Vol. 845, June 2018, pp. 51–92), is computed from the curvature of advected material lines and, for the first time, from high-order numerical derivatives of the wall-normal velocity obtained from direct numerical simulations of a circular cylinder and a cambered NACA 65(1)-412 airfoil. As the spline-based boundary parametrization of the airfoil profile induces oscillations, the principle spiking point can be recovered robustly through appropriate filtering. The short-term kinematics correlate strongly with the scaling lengths in the boundary layer.

I. Introduction

AS PRACTICAL small-scale flying devices proliferate, and as interest in turbomachinery at various scales develops, it becomes increasingly important to understand and characterize flows at moderate Reynolds numbers. In this flow regime, laminar boundary-layer separation, reattachment, and transition result in significant changes of the lift and drag, affecting the performance of the airfoil. The control and prevention of flow separation can therefore yield a substantial extension of the operating range of the device. The dynamics of flow separation are highly nonlinear and make the design of an effective passive and active flow control system challenging.

Although some flow control concepts work by completely removing or reenergizing the separated fluid through suction and blowing (see, e.g., the work of Schlichting and Gersten [1]), other techniques take advantage of instabilities and nonlinearities in the flow by using more compact zero-net-mass-flux (ZNMF) devices such as synthetic jets [2–4]. Given the limited power of these ZNMF instruments, the design of an effective and efficient control strategy should not only focus on directly changing the global events in the flow but rather on understanding and controlling the more subtle and unsteady features of separation.

In steady flows, separation from a no-slip wall is well known to be exactly identified by the Prandtl condition through a point of zero skin friction and a negative friction gradient in the wall-tangential direction. For unsteady flows, similar first-principle criteria were only recently developed by Haller [5]. He proved that, for time-periodic flows, an objective Lagrangian separation point is located at the averaged zero-skin-friction location. Haller further showed that flow separation from a no-slip boundary starts with an upwelling of Lagrangian fluid tracers upstream of the separation point, and that

those particles are drawn toward an unstable manifold in the flow while they are ejected from the wall. This so-called asymptotic separation profile is anchored at the separation point, and it guides fluid particles as they break away in the vicinity of the wall (see the works of Haller [5] and Weldon et al. [6]).

To illustrate this Lagrangian separation behavior, we consider the time-periodic flow over a circular cylinder in Fig. 1. In the figure, a set of fluid particle tracers is initialized in a layer parallel to the cylinder wall and divided in upstream (red) and downstream (blue) groups by the linear approximation of the separation line (green). Also visualized are the instantaneous zero-skin-friction points (green dot) and streamlines (black). As the particles are advected, they undergo an upwelling motion, which is visible through an increasingly sharp spike in the material lines that are initially parallel to the wall. The spikes of particles are asymptotically drawn toward the attracting separation line. Mathematically, these attracting lines are interpreted as unstable manifolds.

In general, stable and unstable manifolds can be identified by extracting ridges in the finite-time Lyapunov exponent (FTLE) fields. These FTLE fields are determined from the maximum deformations in flow maps that are in turn constructed from integrated particle tracer fields in forward and backward times, respectively. The ridges usually demarcate a hyperbolic Lagrangian coherent structure (LCS) [7,8]. Although a hyperbolic Lagrangian coherent structure can be identified through local maxima in the FTLE field, Haller [9] showed that the FTLE field has ridges in regions of high shear that are nonhyperbolic [10].

Even though hyperbolic LCSs are mostly near zero-flux material lines [11], they fall short in the identification of the start of flow separation at the boundary wall. Because of the zero-velocity no-slip condition, the wall is naturally a set of nonhyperbolic fixed points. As a result, the backward-time (attracting) FTLE cannot intersect the wall but envelops the aerodynamic body, as we show for the circular cylinder flow in Fig. 2. The FTLE can hence only identify long-term attracting and repelling surfaces away from the wall rather than the onset of separation.

Based on the initial upwelling and subsequent spike formation described earlier, Serra et al. [12] developed a kinematic methodology to extract the Lagrangian backbone of separation, i.e., the theoretical centerpiece of the forming spike in wall-bounded flows from the analysis of the curvature of material lines. The initial position of the backbone of separation is a wall-transverse ridge of

Received 8 September 2019; revision received 9 December 2019; accepted for publication 20 December 2019; published online 27 March 2020. Copyright © 2020 by Gustaaf Jacobs. Published by the American Institute of Aeronautics and Astronautics, Inc., with permission. All requests for copying and permission to reprint should be submitted to CCC at www.copyright.com; employ the eISSN 1533-385X to initiate your request. See also AIAA Rights and Permissions www.aiaa.org/randp.

*Department of Aerospace Engineering.

†Department of Aerospace Engineering (Corresponding Author).

‡School of Engineering and Applied Sciences.

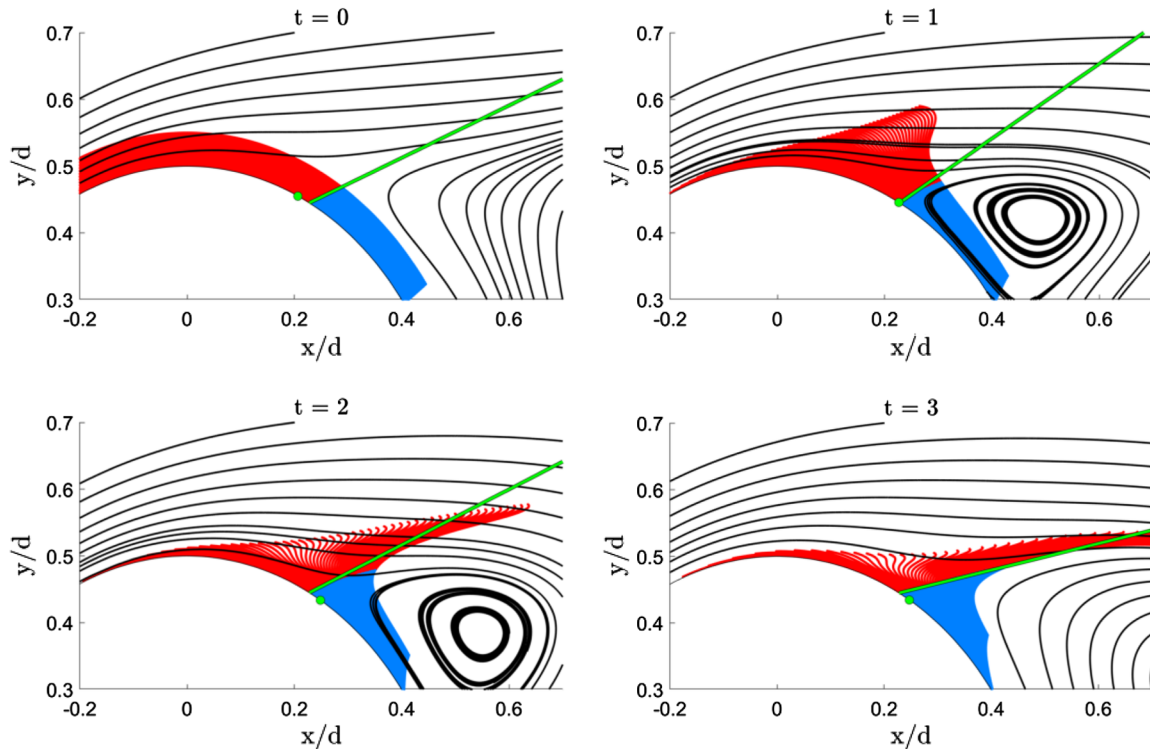


Fig. 1 Snapshots of color-coded particles advected over a circular cylinder near the separation point.

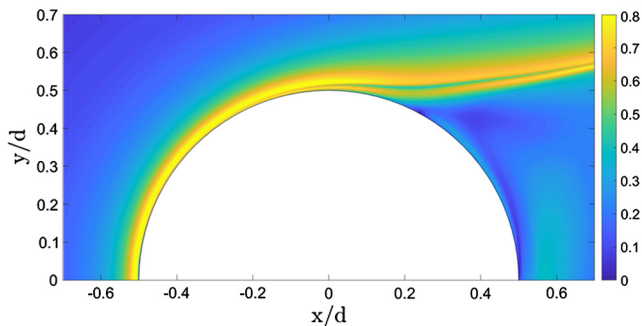


Fig. 2 Backward-time FTLE around the upper-half of a cylinder.

the Lagrangian curvature change field (see the following), whereas the later positions can be captured by materially advecting the initial position with the flow map. If the backbone connects to the wall, we call the separation “on wall” and the intersection point the “Lagrangian spiking point.” This analysis therefore yields a criterion for determining the start of flow separation in the Lagrangian frame. Serra et al. [12] directly related the Lagrangian spiking point to higher-order derivatives of the normal velocity at the wall, and thus provided a criterion for the origin of flow separation in the kinematic sense using only wall-based quantities. In the instantaneous limit, the Lagrangian backbone of separation turns into the Eulerian backbone of separation (Serra et al. [12]). The work on material spike formation was elaborated by Serra et al. [13] for several example flows, including a separation bubble on a flat plate and a rotating cylinder.

In this paper, we present a comprehensive kinematic study of Lagrangian flow separation in external aerodynamics by connecting FTLE dynamics, the asymptotic separation line, and spike formation. Using direct numerical simulations of a circular cylinder flow and the flow over a cambered NACA 65(1)-412 airfoil, we show that, although the motion of fluid particles in the vicinity of the no-slip wall is governed by the spike formation theory (Serra et al. [12]) over short times, as well as over long times by the asymptotic separation profile (Haller [5]), the off-wall kinematics are governed by long-term attracting LCSs in the flowfield that can be extracted from ridges in the backward-time FTLE. We find that the shape of the Lagrangian

backbone of separation attains strong bends along the boundary-layer heights identified through the momentum and displacement thickness. These boundary-layer thickness approximations are based on kinetic arguments and typically involve a threshold value. The purely kinematic Lagrangian backbone of separation, in contrast, is threshold free and consistently distinguishes on- and off-wall regions characterized by different dynamics.

A schematic of the principal mechanisms of separation in steady or periodic flows with an asymptotic mean is presented in Fig. 3. The attracting LCS, which is identified from the backward-time FTLE ridge (blue), attracts the upwelling fluid material (red) from the wall. This ridge does not intersect with the wall, but rather develops along the separated shear layer. The Lagrangian backbone of separation (magenta) is the theoretical centerpiece of the spike and intersects the boundary at the so-called spiking point. Attracted by the hyperbolic LCS, the backbone then aligns with the FTLE ridge once the Lagrangian fluid tracers have left the vicinity of the wall. Downstream of the spiking point, the asymptotic separation profile (green) is anchored at the location of averaged zero skin friction and oriented in the direction of particle breakaway.

We further identify the wall signature of upwelling material lines (i.e., the spiking point [12]) from Lagrangian quantities and, for the first time, from high-order wall-based velocity derivatives. By matching the spiking points extracted from the Lagrangian curvature change of material lines and Eulerian on-wall velocity derivatives of the circular cylinder, we verify the criterion proposed by Serra et al. [12]. The cylinder case benefits from an analytically known boundary with constant curvature. To extend the test to a nonanalytic wall representation, the flow around the airfoil with a cubic-spline-based boundary is analyzed. Although the material lines show the formation of a single

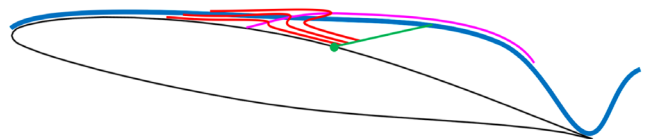


Fig. 3 Schematic of manifolds involved in Lagrangian flow separation: backward-time FTLE (blue), upwelling material lines (red) and associated Lagrangian backbone (magenta), and linear separation profile and asymptotic separation point (green). Schematic not to scale.

spike at midchord characterized by a severe curvature change, very weak curvature ridges occur upstream of the asymptotic location of separation. The higher-order on-wall derivatives reflect these ridges and show their relation to the piecewise linear curvature of the wall. Applying a filter with a kernel based on the distance between supporting points of the spline, we recover the spiking point of the principal separation event from the on-wall velocity derivatives and match the wall intersection of the Lagrangian backbone of separation. The robustness of this method to local oscillations or noise is an important result that will benefit future applications, given that many engineering applications rely on surface representations through splines.

We further show that singular points, such as the stagnation point at the leading edge, must be excluded from the analysis of material spike formation because they can induce fluid upwelling without separation. Barring this limitation, the material spike formation provides wall-based and short-term information that remains hidden in the backward-time FTLE and the asymptotic separation profile. The new information about the material spike adds a valuable piece to the picture of Lagrangian flow separation and is a promising tool in the design of flow controllers.

The governing equations and the numerical model are given in Sec. II. In Sec. III, we outline the setup of our computations, and the results are discussed in the subsequent part. A summary and conclusions are given in Sec. V.

II. Methodology

A. Governing Equations

We consider the compressible Navier–Stokes equations for the conservation of mass, momentum, and energy, which can be written in nondimensional form as a system of equations where the flux vector is divided into an advective part (superscript a) and a viscous part (superscript v):

$$\frac{\partial \mathbf{Q}}{\partial t} + \mathbf{F}_x^a + \mathbf{G}_y^a - \frac{1}{Re_f} (\mathbf{F}_x^v + \mathbf{G}_y^v) = 0 \quad (1)$$

The solution and flux vectors are

$$\mathbf{Q} = [\rho \quad \rho u \quad \rho v \quad \rho E]^T \quad (2)$$

$$\mathbf{F}^a = [\rho u \quad p + \rho u^2 \quad \rho uv \quad u(\rho E + p)]^T \quad (3)$$

$$\mathbf{G}^a = [\rho v \quad \rho vu \quad p + \rho v^2 \quad v(\rho E + p)]^T \quad (4)$$

$$\mathbf{F}^v = \left[0 \quad \tau_{xx} \quad \tau_{yx} \quad u\tau_{xx} + v\tau_{yx} + \frac{\kappa}{(\gamma-1)PrM_f^2} T_x \right]^T \quad (5)$$

$$\mathbf{G}^v = \left[0 \quad \tau_{xy} \quad \tau_{yy} \quad u\tau_{xy} + v\tau_{yy} + \frac{\kappa}{(\gamma-1)PrM_f^2} T_y \right]^T \quad (6)$$

and the equation of state follows as

$$p = \frac{\rho T}{\gamma M_f^2} \quad (7)$$

All quantities are nondimensionalized with respect to a characteristic problem-dependent length scale, reference velocity, density, and temperature yielding the nondimensional Reynolds number Re_f and Mach number M_f .

B. Discontinuous Galerkin Spectral Element Method

On the computational domain, the system of equations [Eq. (1)] is spatially approximated using a discontinuous Galerkin spectral element method (DGSEM) and integrated in time with a fourth-order explicit Runge–Kutta scheme. Gauss–Lobatto quadrature nodes are used for the spatial integration, and a kinetic-energy-conserving split-form approximation of the advective volume fluxes ensures stability of the scheme through cancellation of aliasing errors from the

nonlinear terms. For a detailed description of the scheme, we refer to the works of Kopriva [14], Gassner et al. [15], and Klose et al. [16].

C. Finite-Time Lyapunov Exponent

We extract structures and patterns from flowfield data using a finite-time Lyapunov exponent contour field [11]. The FTLE, which characterizes the maximal stretching of infinitesimal fluid volumes over a given time interval, is determined by tracing fluid particles over time and subsequently computing the deformation tensor induced by the flow map.

We express the particle trajectories as

$$\mathbf{x}(\mathbf{x}_0, t_0; T) = \mathbf{x}_0 + \int_{t_0}^{t_0+T} \mathbf{v}(\mathbf{x}(\tau; \mathbf{x}_0, t_0), \tau) d\tau \quad (8)$$

from which the flow map \mathbf{F} is defined:

$$\mathbf{F}_{t_0}^t(\mathbf{x}_0, t_0; T) \equiv \mathbf{x}(\mathbf{x}_0, t_0; T) \quad (9)$$

From the deformation gradient tensor $\nabla \mathbf{F}_{t_0}^t$, the right Cauchy–Green strain tensor $\mathbf{C}_{t_0}^t = [\nabla \mathbf{F}_{t_0}^t]^* \nabla \mathbf{F}_{t_0}^t$ can be used to compute the strain in the Lagrangian frame. With the largest eigenvalue of the strain tensor $\lambda_2(\mathbf{C}_{t_0}^t(\mathbf{x}_0))$, the finite-time Lyapunov exponent field is defined as

$$\Lambda_{t_0}^t(\mathbf{x}_0) = \frac{1}{|t - t_0|} \ln \sqrt{\lambda_2(\mathbf{x}_0)} \quad (10)$$

This FTLE identifies the highest Lagrangian rate of stretching in the flowfield. Tracing fluid particles forward or backward in time, ridges of the FTLE field can be used to identify hyperbolic repelling and attracting Lagrangian coherent structures (see the works of Haller [7,9] and Nelson and Jacobs [17] for a more detailed description).

Although ridges in the backward-time FTLE are associated with separation (see the work of Mohseni et al. [18]), the no-slip condition makes the wall a set of nonhyperbolic fixed points, inhibiting any transverse intersections with FTLE ridges. Furthermore, the birth of a material spike is not a stretching-dominated phenomenon but rather the outcome of an interplay of stretching and rotation objectively captured by the material curvature (Serra et al. [12]). The strain-based FTLE field is therefore not suited to detect the start of Lagrangian flow separation on no-slip boundaries.

D. Separation Point and Angle

Haller [5] showed that, for flows with an asymptotic mean (such as periodic flows), the asymptotic separation point γ is located at the integrated zero-skin-friction point:

$$\frac{1}{t_1 - t_0} \int_{t_0}^{t_1} c_f(\gamma, t) dt = 0 \quad (11)$$

Haller [5] further derived an analytic expression for the separation profile, which is a wall-bounded unsteady manifold along which fluid particles are ejected from the wall into the freestream. The slope, or separation angle, of this line can be computed just by evaluating integrated values of the pressure and skin-friction data at the wall:

$$\tan(\alpha(t_0)) = - \lim_{T \rightarrow \infty} \frac{3 \int_{t_0}^T \tau_x(\gamma, t) dt}{\int_{t_0}^T [p_x(\gamma, y_w, t) + 3\tau_x(\gamma, t) \int_{t_0}^t (1/\mu)\tau(\gamma, s) ds] dt} \quad (12)$$

Here, the x coordinate refers to wall-tangential direction, and y points in the wall-normal direction. The separation angle α is the angle to the tangent of the wall at the separation point. Using both the separation point and the separation angle, a linear approximation of the separation profile can be constructed.

E. Lagrangian Backbone of Separation and the Spiking Point

Flow separation is invariably characterized by the ejection of fluid particles from a no-slip wall. Although the long-time (asymptotic) behaviors of these particles are governed by attracting LCSs in the flowfield, the onset of separation is not related to asymptotic structures. Serra et al. [12] showed that the formation of a material spike is characterized by high folding induced by the flow on material lines close to the wall (Fig. 3), which appears at a different location (generally upstream) as compared to the asymptotic separation point (e.g., the zero-skin-friction point in the case of steady flows). This deformed spike then eventually converges to the breakaway from the wall along the corresponding long-term separation structure. The materially evolving set of points forming the centerpiece of the separation spike (magenta curve in Fig. 3) is also referred to as the backbone of separation [12].

Following Serra et al. [12], separation is on wall if the backbone has a transverse intersection with the nonslip boundary, and it is off wall otherwise. We note that such a distinction is not postulated a priori based on heuristic arguments, but rather is an outcome of the theory proposed in Ref. [12]. Using a coordinate system $[s, \eta]$ in the directions tangential and normal to the wall, respectively, we compute the Lagrangian curvature change relative to the initial curvature

$$\bar{\kappa}_{t_0}^{t_0+T} := \kappa_{t_0}^{t_0+T} - \kappa_0 \quad (13)$$

in a neighborhood of the no-slip boundary foliated by a set of material lines initially parallel to the wall and parametrized by $\mathbf{r}_\eta(s)$, $s \in [s_1, s_2] \subset \mathbb{R}$, and $\eta \in [0, \eta_1] \subset \mathbb{R}$. Such a foliation enslaves the initial local tangent \mathbf{r}'_η and curvature κ_0 to the position \mathbf{r}_η , therefore making $\bar{\kappa}_{t_0}^{t_0+T}$ a function of t_0 , T , and of the initial configuration \mathbf{r}_η only. Here, $(\cdot)' := (d/ds)(\cdot)$. The $\bar{\kappa}_{t_0}^{t_0+T}$ field can be directly computed from the flow map $\mathbf{F}_{t_0}^{t_0+T}$ using the relation

$$\begin{aligned} \bar{\kappa}_{t_0}^{t_0+T} = & \frac{\langle (\nabla^2 \mathbf{F}_{t_0}^{t_0+T}(\mathbf{r}_\eta) \mathbf{r}'_\eta) \mathbf{r}'_\eta, \mathbf{R} \nabla \mathbf{F}_{t_0}^{t_0+T}(\mathbf{r}_\eta) \mathbf{r}'_\eta \rangle}{\langle \mathbf{r}'_\eta, \mathbf{C}_{t_0}^{t_0+T}(\mathbf{r}_\eta) \mathbf{r}'_\eta \rangle^{3/2}} \\ & + \kappa_0 \left[\frac{\det(\nabla \mathbf{F}_{t_0}^{t_0+T}(\mathbf{r}_\eta)) \langle \mathbf{r}'_\eta, \mathbf{r}'_\eta \rangle^{3/2}}{\langle \mathbf{r}'_\eta, \mathbf{C}_{t_0}^{t_0+T}(\mathbf{r}_\eta) \mathbf{r}'_\eta \rangle^{3/2}} - 1 \right] \end{aligned} \quad (14)$$

where $\langle \cdot, \cdot \rangle$ denotes the inner product;

$$(\nabla^2 \mathbf{F}_{t_0}^{t_0+T}(\mathbf{r}_\eta) \mathbf{r}'_\eta)_{ij} = \sum_{k=1}^2 \partial_{jk} \mathbf{F}'_{t_0}(\mathbf{r}_\eta) \mathbf{r}'_{\eta k}, \quad i, j \in \{1, 2\} \quad (15)$$

and \mathbf{R} is the rotation matrix defined as

$$\mathbf{R} := \begin{bmatrix} 0 & 1 \\ -1 & 0 \end{bmatrix} \quad (16)$$

We note that, with a clockwise parametrization of the no-slip boundary, $\mathbf{R} \mathbf{r}'_\eta$ is the vector normal to the initial material line, pointing toward the boundary. The initial position $\mathcal{B}(t_0)$ of the Lagrangian backbone of separation (i.e., the theoretical centerpiece of the material spike over $[t_0, t_0 + T]$) is then defined as a positive-valued wall-transverse ridge of the $\bar{\kappa}_{t_0}^{t_0+T}$ field (see the work of Serra et al. [12] for details). The later position of the backbone $\mathcal{B}(t)$ can be computed by materially advecting $\mathcal{B}(t_0)$, i.e., letting

$$\mathcal{B}(t) := \mathbf{F}_{t_0}^t(\mathcal{B}(t_0)), \quad t \in [t_0, t_0 + T] \quad (17)$$

If $\mathcal{B}(t_0)$ connects to the wall transversally, the intersection point is called the Lagrangian spiking point and is defined by

$$(s_p, 0) := \mathcal{B}(t_0) \cap \text{no-slip wall} \quad (18)$$

Serra et al. [12] also derived alternative exact formulas for the Lagrangian spiking point using only on-wall Eulerian quantities in

Table 1 Equations determining Lagrangian spiking point $(s_p, 0)$ for generally aperiodic compressible (left) and incompressible (right) flows on a no-slip boundary in terms of on-wall Eulerian quantities^a

$\nabla \cdot \mathbf{v} \neq 0$	$\nabla \cdot \mathbf{v} = 0$
$\begin{cases} \int_{t_0}^{t_0+T} \partial_{ss\eta\eta} \hat{v}(s_p, 0, t) = 0, \\ \int_{t_0}^{t_0+T} \partial_{ss\eta\eta} \hat{v}(s_p, 0, t) > 0, \\ \int_{t_0}^{t_0+T} \partial_{ss\eta\eta} \hat{v}(s_p, 0, t) < 0 \end{cases}$	$\begin{cases} \int_{t_0}^{t_0+T} \partial_{ss\eta\eta} \hat{v}(s_p, 0, t) = 0, \\ \int_{t_0}^{t_0+T} \partial_{ss\eta\eta} \hat{v}(s_p, 0, t) > 0, \\ \int_{t_0}^{t_0+T} \partial_{ss\eta\eta} \hat{v}(s_p, 0, t) < 0 \end{cases}$

^a \hat{v} indicates the velocity direction normal to the wall.

the case of steady, time-periodic, and generally aperiodic flows (cf. Table 1). Finally, in the instantaneous limit ($T = 0$), the Lagrangian backbone of separation and the spiking point turn into their correspondent Eulerian versions (Serra et al. [12]).

In Table 1, \hat{v} indicates the velocity in the normal direction to the wall, and it can be computed from the inner product:

$$\hat{v} = \langle \mathbf{v}, \mathbf{n} \rangle = u n_x + v n_y, \quad \mathbf{n} := \mathbf{R} \frac{\mathbf{r}'_\eta}{|\mathbf{r}'_\eta|}, \quad |\mathbf{r}'_\eta| = \sqrt{\langle \mathbf{r}'_\eta, \mathbf{r}'_\eta \rangle} \quad (19)$$

Assuming a curved, parametrized boundary $\mathcal{W}(s)$, the normal vector \mathbf{n} at each collocation point \mathbf{x}_i is the vector pointing to the closest intersection point with the boundary \mathcal{W} and is found by minimizing the distance function $d_i(s) = |\mathbf{x}_i - \mathcal{W}(s)|$. If we assume a continuous and sufficiently smooth function \hat{v} , we can switch the order of differentiation in Table 1 and compute the normal gradients first. Once the normal velocity is obtained at each collocation point, the gradient can be computed by multiplication with the derivative matrix \mathcal{D} . Using the spectral operator \mathcal{D} gives the derivatives in x and y directions in the polynomial order of the scheme:

$$\nabla \hat{v} = \mathcal{D} \hat{v} \quad (22)$$

The directional derivative of the normal velocity \hat{v} in the direction of the wall-normal vector \mathbf{n} is computed as

$$\partial_\eta \hat{v} = \nabla_n \hat{v} = \nabla \hat{v} \cdot \mathbf{n} = (\partial_x \hat{v}) n_x + (\partial_y \hat{v}) n_y \quad (23)$$

This relation allows us to calculate the normal derivatives everywhere in the flowfield from the velocity gradient and the normal vector at each point. Once $\partial_\eta \hat{v}$ or $\partial_{\eta\eta} \hat{v}$ are determined, they can be projected onto the boundary, and the derivatives tangential to the wall can be computed subsequently as one-dimensional operations.

III. Problem Setup

The canonical circular cylinder flow is computed at a Reynolds number of $Re_d = 100$ based on a cylinder diameter of unity and a Mach number of 0.1, rendering compressibility effects negligible. The computational domain is divided into 347 quadrilateral elements (see Fig. 4), and the solution is approximated with a 16th-order polynomial. This accounts for a total of 100,283 collocation points. At the outer boundaries, a freestream condition is applied, whereas the cylinder is approximated with curved element faces and an adiabatic no-slip wall. A Riemann solver is used to sort out the characteristic relations at the boundaries [19,20]. Note that 402,201 Lagrangian particles are initialized in 201 wall-parallel lines around the cylinder with a spacing of $\Delta/d = 0.001$ between each line.

The flow over a NACA 65(1)-412 airfoil is simulated at a Reynolds number based on the chord length of $Re_c = 20,000$ and a Mach number of $M = 0.3$. The Mach number is relatively low, ensuring a nominally incompressible flow, but it is high enough to prevent stability issues pertaining to the explicit time integration we use. The computational domain is given in Fig. 5 and consists of 2,256 quadrilateral elements, with the dimensions of the domain being adopted from the work of Nelson et al. [21], who showed that the solution is not significantly affected by the domain size. Boundary conditions at the outer edges of the computational domain are

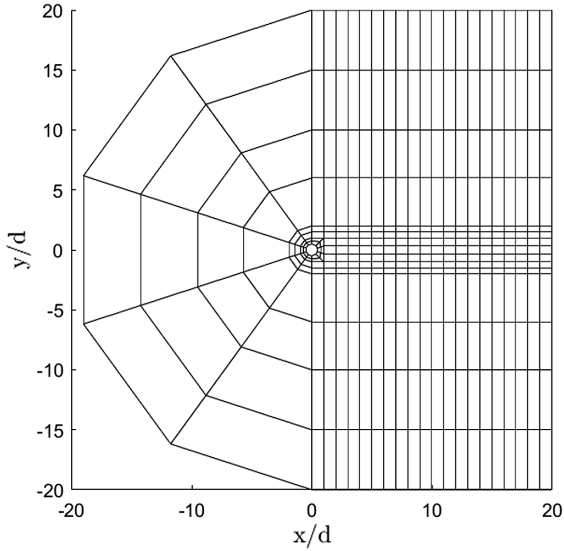


Fig. 4 Two-dimensional (2-D) computational domain for circular cylinder.

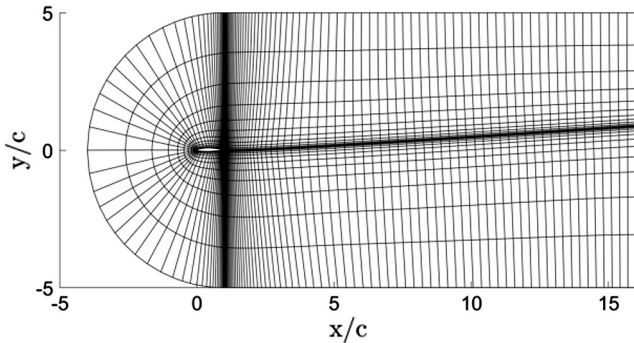


Fig. 5 2-D computational domain for NACA 65(1)-412. Only elements without interior Gauss–Lobatto nodes shown.

specified as freestream boundaries, whereas the airfoil surface is treated as a nonslip, adiabatic wall. The wall-boundary elements are curved and fitted to a spline representing the airfoil's surface according to Nelson et al. [21]. Again, the characteristic relations at the boundaries are sorted out by using a Riemann solver. The solution vector is approximated with a 16th-order polynomial, giving a total of 651,984 collocation points in the domain. Note that 1,005,201 Lagrangian particles are initialized in 201 wall-parallel lines around the airfoil with a spacing of $\Delta/c = 0.0002$ between each line.

In both simulations, Lagrangian particles are tracked by spectrally interpolating the velocity field for each particle and numerically integrating $\dot{\mathbf{x}}(\mathbf{x}, t) = \mathbf{v}(\mathbf{x}(t), t)$ using a third-order Adam–Bashfort scheme. Efficient particle tracking and velocity interpolation is performed as described by Mittal et al. [22]. Once the Lagrangian curvature change field [Eq. (14)] is calculated, a basic smoothing operation is performed to filter out numerical noise.

The wall-normal derivatives in Table 1 are computed within the DGSEM solver. With Eqs. (21) and (23), the quantities \hat{v}_η and $\hat{v}_{\eta\eta}$ can be spectrally computed in each element using the operators available in the DGSEM framework and subsequently projected onto the wall using Lagrange interpolating polynomials. The derivatives in the wall-tangential direction can either be computed within the DGSEM solver or as part of the postprocessing work. Given that numerical noise is strongly amplified when computing higher derivatives, a smoothing filter is applied to the direct numerical simulation output data as a postprocessing step.

IV. Results and Discussion

A. Cylinder Flow

To study the kinematics of flow separation, we consider a cylinder flow at $Re_d = 100$. Ridges in the FTLE field show a flow pattern that

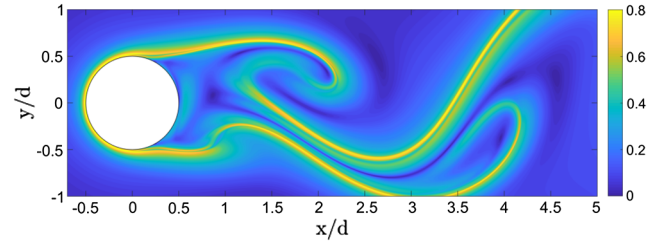


Fig. 6 Backward-time FTLE from integration over one vortex shedding period.

is well known to be dominated by a pair of counter-rotating vortices alternately shedding in a regular manner from the top and bottom of the cylinder with a period of approximately six convective time units [23,24]. A snapshot of the backward-time FTLE (Fig. 6) reveals the long-term attracting LCSs in the wake, which highlight the edges of the advected vortices. Although this LCS is associated with separation (see the work of Mohseni et al. [18]) and with early vortex formation and shedding [24], the FTLE ridge cannot intersect with the cylinder wall but rather envelopes the body. This is a direct consequence of the no-slip condition at the wall and nonhyperbolicity, as was explained in the Introduction (Sec. I). The exact on-wall origin of separation can hence not be identified solely based on a strain-based FTLE field. A more rigorous analysis of the near-wall flowfield is required. To this end, we first determine the asymptotic separation point and line [5], and then we compute the Lagrangian curvature change $\bar{\kappa}_{t_0}^{t_0+T}$ and associated spiking dynamics. Later, we will relate the material spiking and the FTLE.

The averaged zero-skin-friction point is determined according to Eq. (11) with the temporal mean of the skin-friction coefficient over one vortex shedding period. It is located at $x/d = 0.23$, which is approximately halfway between center and the rear end of the cylinder. The angle of the separation line with respect to the tangent of the cylinder surface at the separation point is determined with Eq. (12). It oscillates periodically between 34 and 57 deg. We use the angle and the separation point to create a linear approximation of the unstable manifold to which fluid particles that eject from the wall are asymptotically attracted.

The near-wall dynamics are visualized in Fig. 7, where color-coded fluid tracers, the linear separation profile, and instantaneous streamlines are plotted for different integration times T . In the figure, particles are divided in upstream (red) and downstream (blue) groups by the linear approximation of the separation line (green). Also visualized are the instantaneous zero-skin-friction points (green dot) and streamlines (black). Particles up- and downstream of the line undergo an initial upwelling (spiking) and are drawn toward the unstable manifold.

To identify the onset of flow separation (i.e., the origin of material spiking), we extract a backbone from the evolution of the material lines through ridges in the corresponding advected curvature field $\bar{\kappa}_{t_0}^{t_0+T}$. We plot the curvature field for integration times of $T = [0.1, 0.4, 0.7, 1.0]$ and $t_0 = 0$ in Fig. 8. Note that we first compute $\bar{\kappa}_{t_0}^{t_0+T}$, which is a scalar field based at t_0 ; and then we advect it with $\mathbf{F}_{t_0}^{t_0+T}$. The latter operation reflects the material property of lines and the backbone:

$$\mathcal{B}(t_0 + T) := \mathbf{F}_{t_0}^{t_0+T}(\mathcal{B}(t_0)) \quad (24)$$

The backbone $\mathcal{B}(t)$ is shown in magenta. For reference, we also plot the instantaneous zero-skin-friction point and the linear approximation of the separation profile in green.

The evolution of material lines in Fig. 8 shows that the backbone profile $\mathcal{B}(t)$ is correctly placed along the local spikes of material lines and intersects with the wall shortly upstream of the center of the cylinder. The separated fluid tracers then follow the direction of the linearly approximated separation profile. Although the asymptotic separation profile provides information about the long-term behavior of separating fluid tracers, the initial material spike formation

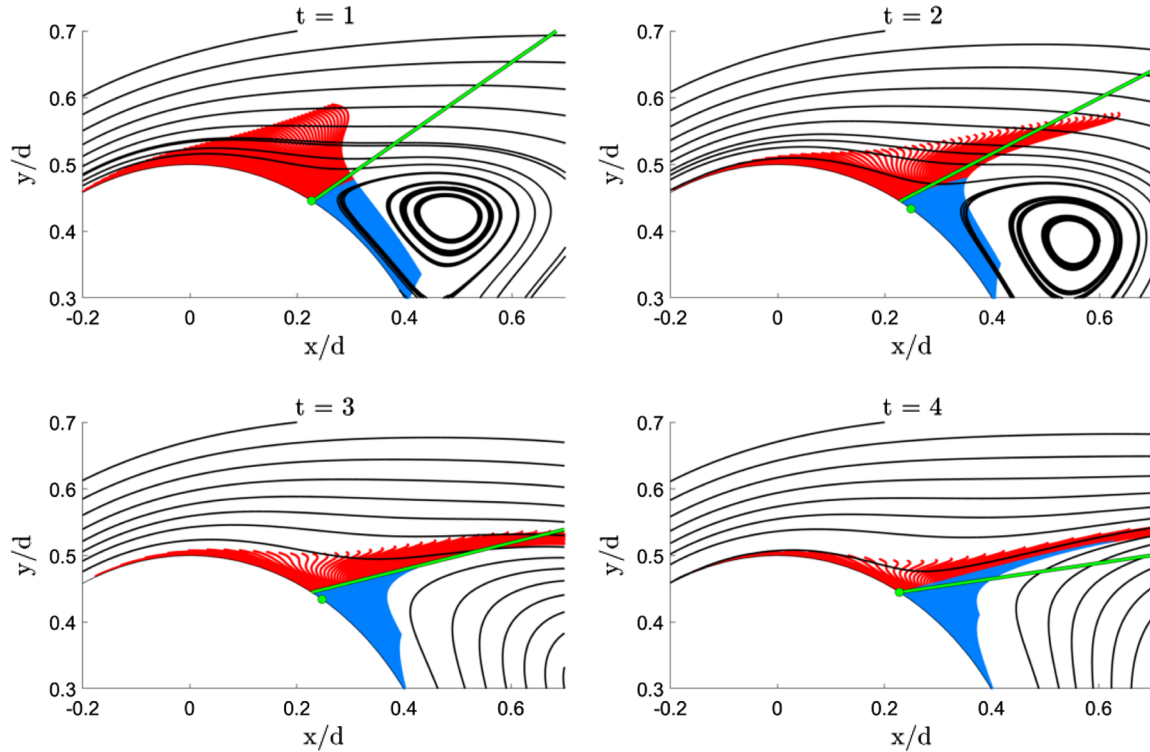


Fig. 7 Snapshots of color-coded particles advected over a circular cylinder near the separation point.

remains hidden and can only be extracted from analysis of the curvature scalar field.

The curvature change field $\bar{\kappa}_{t_0+T}^{t_0+T}$ for integration time intervals of $T = 0.4$ and 1.0 in Fig. 9 reveals a total number of four Lagrangian backbones. Two originate from the top and the bottom of the cylinder; and they evolve along a dominant, growing ridge in the curvature field driven by the separation of the boundary layer. The two other backbones are located within the recirculation region in the separated cylinder wake. They are based on much weaker curvature ridges, and we therefore deem them of secondary interest in the onset of separation.

1. Spiking Phenomenon and FTLE

The spike formation, which occurs over a short time, is hidden to the FTLE field [12]. For longer integration times, however, the material spike (governed by off-wall dynamics) converges to the attracting backward-time FTLE ridge (Fig. 3). For the cylinder case, we visualize the spatial relation between the backbone, material lines, and the backward-time FTLE field at different time instances in Fig. 10. In this figure, a time interval of one vortex shedding period ($T = 6$) is used to compute the FTLE field. Material lines and the backbone are advected from $t = 0$ to $t = 1, 2, 3$, and 4 (black).

Initially, the fluid tracers undergo an upward motion in the transverse direction to the cylinder, and the backbone along the material spike crosses the FTLE ridge ($t = 1$). As the integration time increases, however, the material lines bend downward ($t = 2$) and gradually align with the unstable manifold for $t \geq 3$. The long-term manifold identified through the backward-time FTLE ridge attracts the separating fluid material and gradually aligns with the material backbone. The trace of the separated fluid in the wake follows the same pattern and shows long-term sharp spikes along dominant FTLE ridges, as illustrated in Fig. 11.

The aforementioned results highlight that the Lagrangian backbones of separation and the FTLE provide critical complementary structures in the analysis of Lagrangian flow separation. Although the initial motion through the upwelling of fluid material can only be determined through the analysis of the curvature change field [12], the long-term off-wall dynamics are governed by the FTLE. A combination of both methodologies therefore, together with the

asymptotic separation line, gives a complete picture of the kinematics of separation (see Fig. 3).

2. Extraction of Spiking Points

The spiking points s_p are the wall signatures of material upwelling and can either be identified from the intersection of a wall-transverse curvature change ridge with the boundary [Eq. (18)] or from on-wall Eulerian derivatives of the wall-normal velocity (Table 1). Here, we extract s_p using the criterion for incompressible flows because the flow with a freestream Mach number of $M = 0.1$ is nearly incompressible.

From the condition specified in Table 1, the spiking points are located at the minima of the integrated derivatives of the normal velocity in the normal and tangential direction, $\partial_{\eta_{ss}} \hat{v}$.

We plot this function in Fig. 12a for the upper-half of the cylinder and an interval of $T = 1$. The resulting spiking points are indicated with red circles. Figure 12b shows the curvature change field $\bar{\kappa}_0^1$ and the Lagrangian backbones of separation $\mathcal{B}(t_0)$ in magenta. The spiking points identified from the normal velocity derivatives are plotted as red dots at the boundary and match exactly with the intersection of the backbones and the wall. Through the agreement of the spiking points determined from Eulerian on-wall quantities and the alternative Lagrangian definition [Eq. (18)], here, we verify the theory by Serra et al. [12] for the first time, i.e., we confirm the theory that material upwelling in the Lagrangian frame can also be captured by using wall-based Eulerian quantities only.

Figure 13 shows the curvature change field, based at the initial time, on the upper side of the cylinder for increasing integration times, together with the Lagrangian spiking points from on-wall quantities (red), backbones of separation (magenta), and boundary-layer approximations based on the momentum and displacement thickness in gray and black, respectively. These plots are based on the same particle trace that is used in the previous figures (Figs. 8, 9, and 12b). The Lagrangian spiking point s_p is located at $x/d = -0.09$, which places it far upstream of the asymptotic separation point ($x/d = 0.23$) and, remarkably, even upstream from the cylinder center.

We find that there is a strong correlation between the curvature change field and the boundary-layer scaling thicknesses, such as the displacement thickness and momentum loss thickness [1]. Figure 13

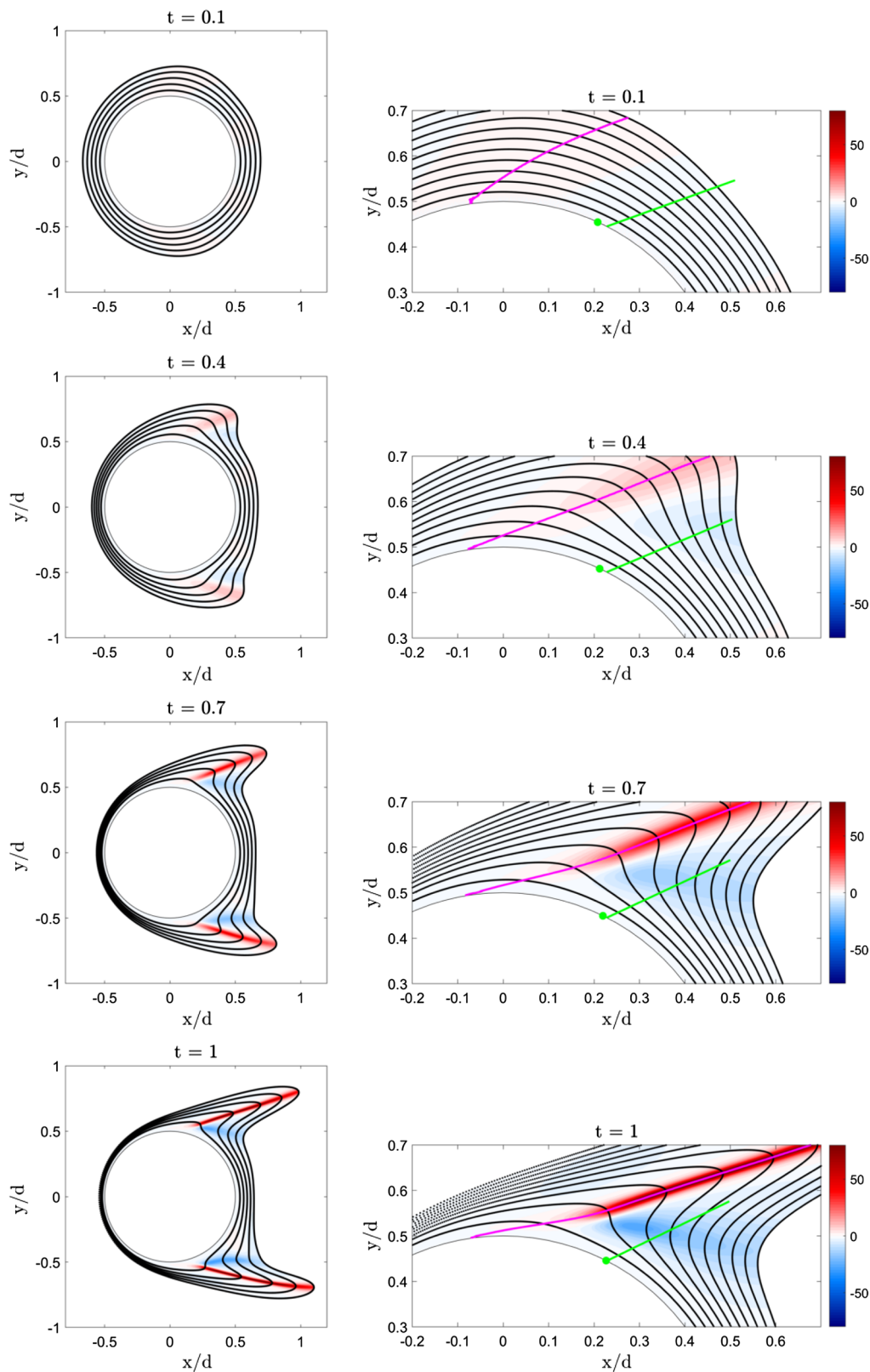


Fig. 8 Advection of material lines and curvature field $\bar{\kappa}_{t_0}^t$, $t = t_0 + T$ around a cylinder for different integration times: backbone $\mathcal{B}(t)$ (magenta), linear separation line and zero-skin-friction point (green).

shows that, as the integration time increases, ridges of $\bar{\kappa}_{t_0}^{t_0+T}$ form and develop a peak at the intersection with the displacement thickness (black line). Within the momentum thickness layer (gray line), the curvature of the ridge abruptly decreases. The dependence of the backbone of separation on the displacement and momentum thickness is a remarkable result because boundary-layer thicknesses follow kinetic arguments and typically involve threshold parameters.

Inflection of the backbone of separation, in contrast (despite being threshold free and purely kinematic), accurately separates on- and off-wall regions characterized by different dynamics. We are currently exploring this correlation in material, and we plan to report on this in the near future.

We note that, even though the curvature change ridge develops a “nose” and moves upstream with increasing integration time,

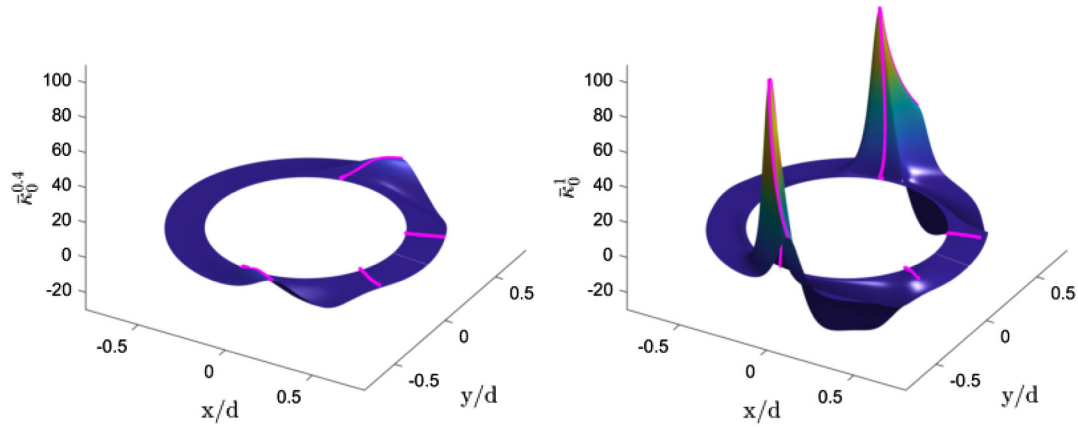


Fig. 9 Surface plot of the curvature scalar fields $\bar{\kappa}_0^{0.4}$ and $\bar{\kappa}_0^1$. Backbone of separation in magenta.

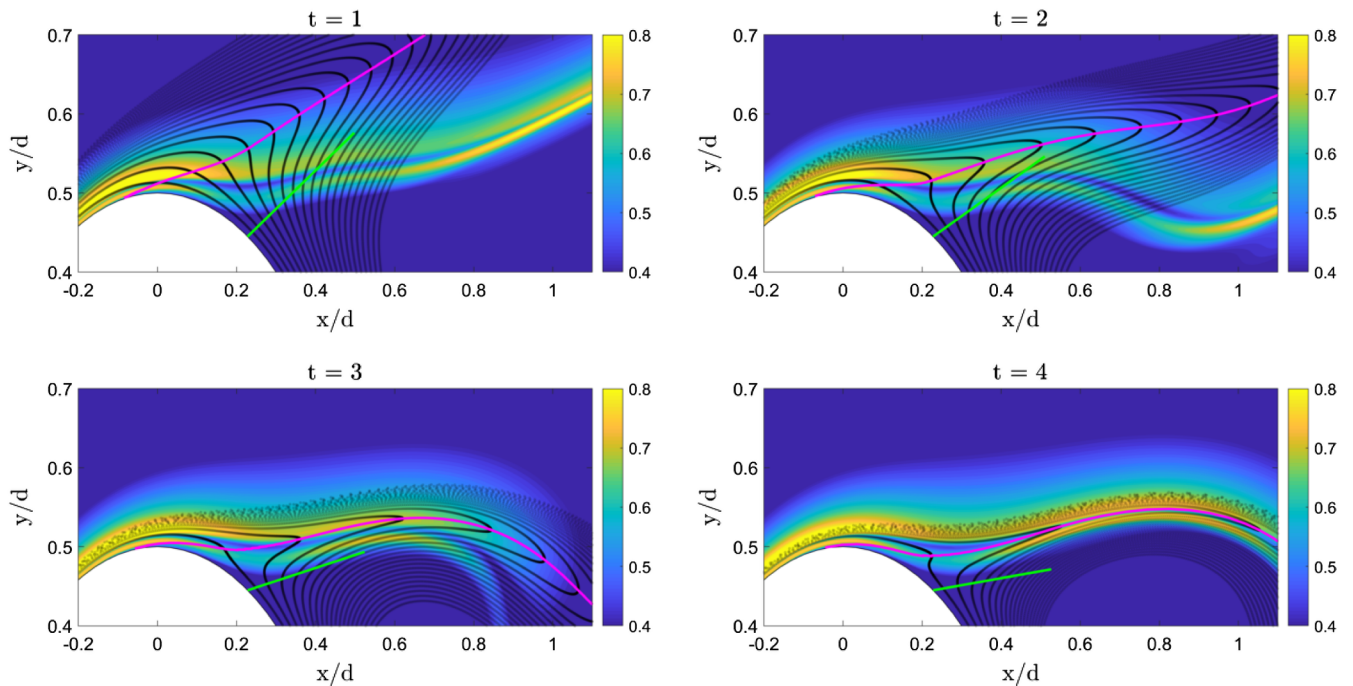


Fig. 10 Backward-time FTLE field (contour plot) computed from t to $t - T$ over $T = 6$: advected material lines from zero to t (black), Lagrangian backbone of separation (magenta), and asymptotic separation profile (green). Y axis stretched.

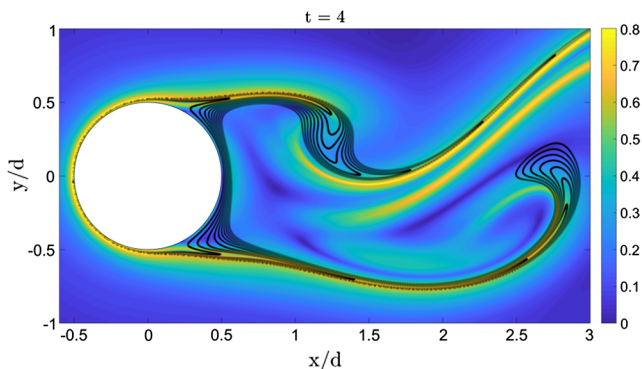


Fig. 11 Backward-time FTLE and material lines in the wake.

the backbone $\mathcal{B}(t_0)$ maintains its original on-wall signature and intersects the wall at the spiking points identified by the criteria in Table 1.

B. Airfoil Flow

For a more complex and encompassing external aerodynamics test case, we study the kinematics of flow separation on a cambered

NACA 65(1)-412 airfoil at a chord-based Reynolds number of $Re_c = 20,000$ and a 4 deg angle of attack. The low-Reynolds-number airfoil flow is characterized by boundary-layer separation at midchord, a recirculation region downstream of the separation location, and a von-Kármán-type vortex shedding in the wake, resulting in a time-periodic flow pattern with a period of $T = 0.36$ convective time units.

A snapshot of the backward-time FTLE (Fig. 14) visualizes the separated shear layer and the edges of the shedded and advected vortices.

The asymptotic separation point is computed using the mean over one vortex shedding period, and it is located at the averaged zero-skin-friction point at $x/c = 0.50$, i.e., exactly at midchord and slightly behind the maximum thickness location of the airfoil ($x/c = 0.4$). This is in accordance with the result reported by Nelson et al. [21] and Kamphuis et al. [25]. The angle of the separation line with respect to the tangent of the airfoil surface periodically oscillates between 7.05 and 7.5 deg. These near-wall dynamics are summarized in Fig. 15, where color-coded fluid tracers, the asymptotic separation profile, and instantaneous streamlines are plotted for different integration times. Similar to the cylinder flow, the particles upstream of the asymptotic separation point undergo an upwelling motion and form a sharp spike that will be later guided by an attracting LCS in the flow.

The advected curvature change field at the final time, together with a set of material lines, is shown in Fig. 16 for different integration

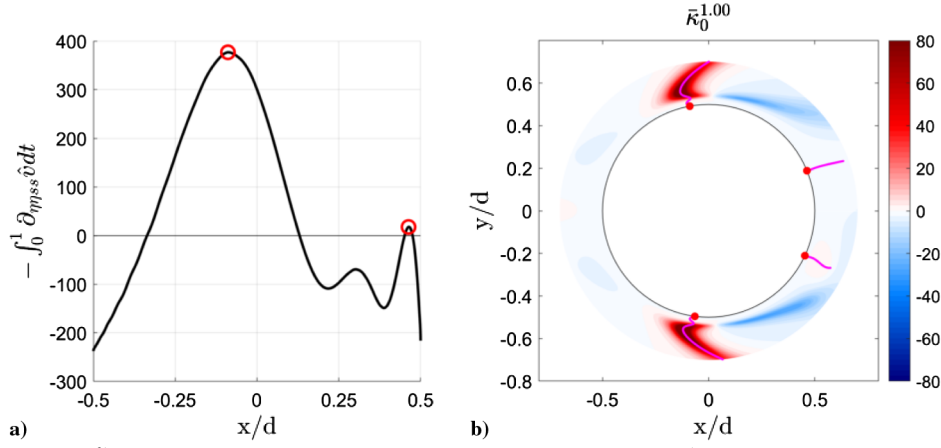


Fig. 12 Representations of a) $-\int_0^1 \partial_{\eta_{ps}} \hat{v} dt$ with spiking points in red, and b) curvature change field $\bar{\kappa}_0^1$ with backbones (magenta) and Lagrangian spiking points (red) identified from Eulerian on-wall quantities.

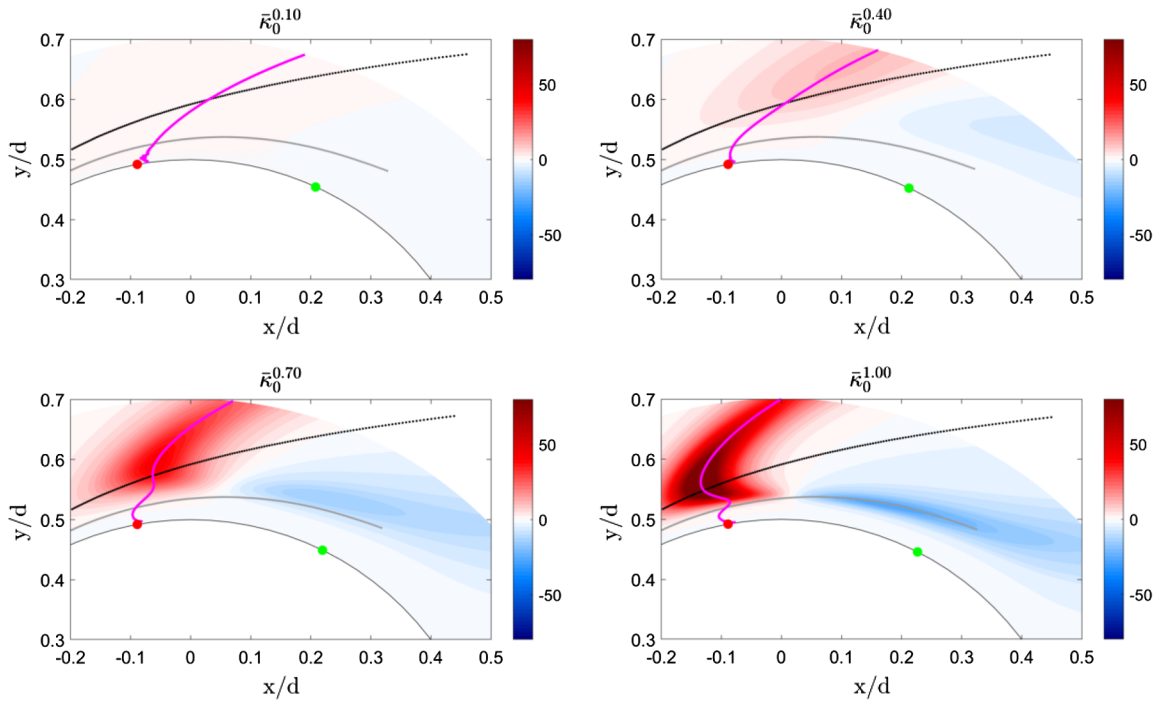


Fig. 13 Lagrangian curvature change field of the circular cylinder with corresponding backbone of separation (magenta) and Lagrangian spiking points (red) identified from Eulerian on-wall quantities for different integration times. Zero-skin-friction point (green), boundary-layer displacement thickness (black) and momentum thickness (gray).

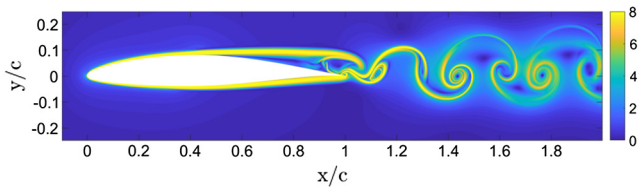


Fig. 14 Backward-time FTLE from integration over one vortex shedding period.

times. Multiple spikes emerge on the suction side of the airfoil: a dominant ridge evolves along the separating shear layer, and several smaller spikes appear within the separated recirculation region. On the pressure (bottom) side, the flow remains attached and the fluid tracers are advected without breaking away from the boundary until the trailing edge is reached. Given that global separation occurs only on the suction side of the airfoil, we focus our analysis on the upper section of the profile. A magnified view of the curvature scalar field introduced in Fig. 16, together with the backbone of separation $B(t)$

and the asymptotic separation profile, is given in Fig. 17. Note that the y axis is stretched to aid the visibility of subtle features.

The backbone emerging at midchord is based on the upwelling of separating material lines in the vicinity of the asymptotic separation line and intersects the no-slip wall at $s_p/c = 0.46$. This location is slightly upstream of the asymptotic separation point at $x/c = 0.5$. Additional curvature ridges are detected within the separated recirculation region but, given that the boundary layer has already separated, are of little interest for determining the start of Lagrangian flow separation.

1. Spiking Phenomenon and FTLE

The relation between the Lagrangian backbone of separation, material lines, and the backward-time FTLE field is illustrated in Fig. 18 at different snapshots in time. To determine the backward-time FTLE field, again, we use an integration time interval equal to one vortex shedding period ($T = 0.36$). Material lines (black) and backbones (magenta) are advected forward in time from $t = 0$ to $t = 0.05, 0.1, 0.2, 0.3, 0.4$, and 0.5 .

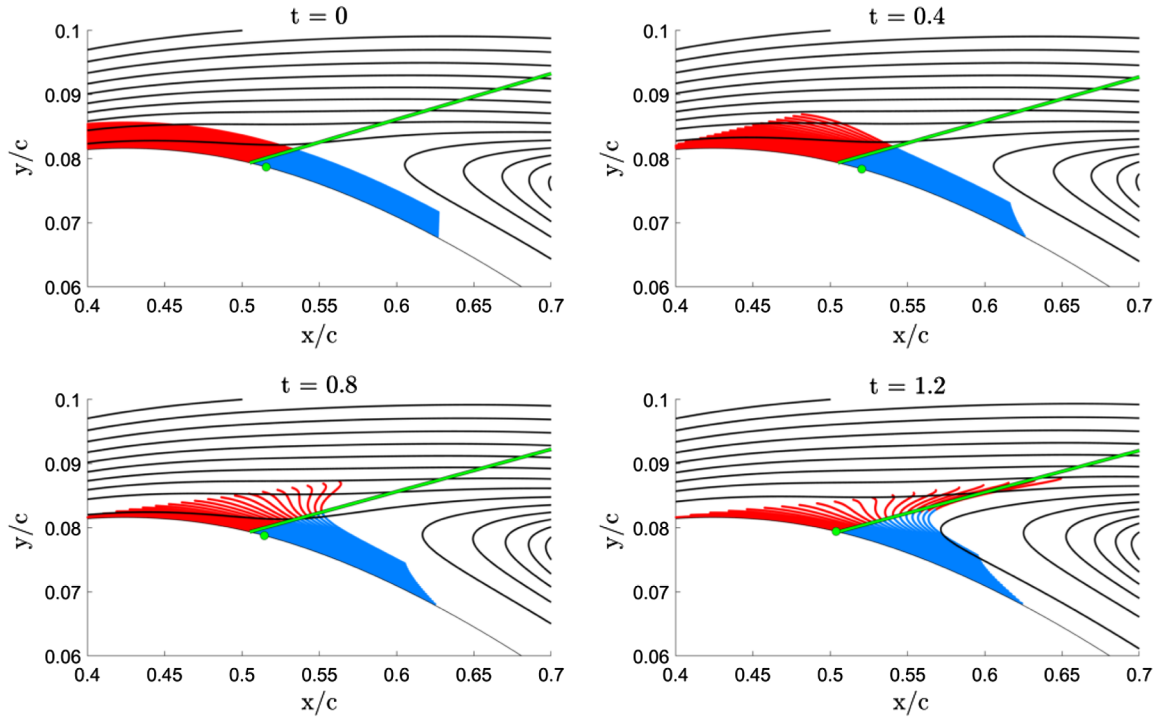


Fig. 15 Snapshots of particles advected over airfoil near asymptotic separation point. Particles divided by asymptotic linear separation line (green) in upstream (red) and downstream (blue) groups. Instantaneous zero-skin-friction points plotted as green dots and streamlines in black.

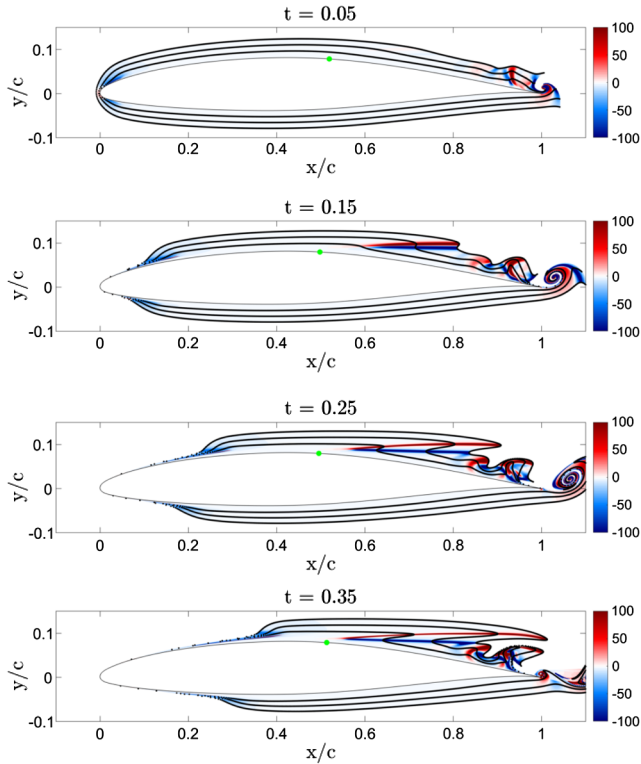


Fig. 16 Advection of material lines and the curvature field $\tilde{\kappa}_{t_0}^{t_0+T}$ around airfoil for different integration times. Zero-skin-friction point in green.

Similar to our findings for the cylinder flow, the material spike starts from the no-slip wall, crossing the FTLE ridge at short-time scales. As the integration time increases, the material spike (along with the backbone of separation) aligns to the attracting FTLE ridge, which again governs the off-wall dynamics of the separated fluid tracers. The separation picture is then completed by the asymptotic

separation line (green) and its connection to the backward-time FTLE ridge (see Fig. 18).

2. Extraction of Spiking Points

We extract the spiking points of the separating airfoil flow from both their Lagrangian and wall-based Eulerian definitions. The curvature change field $\tilde{\kappa}_{t_0}^{t_0+T}$ is given in Fig. 19 for three different integration intervals in x and η coordinates, where η is the wall-normal distance. Besides the large ridges at midchord and at $x/c \approx 0.75$, a weak waviness in the curvature field exists upstream of the asymptotic separation point ($x/c = 0.5$). This oscillatory pattern is recovered in the Eulerian wall derivative $\partial_{\eta_{ss}} \hat{v}$ shown as black line in Fig. 20a.

According to the conditions specified in Table 1, spiking points are located at local minima of the time integral of $\partial_{\eta_{ss}} \hat{v}$, which identifies three locations upstream of the separation point in Fig. 20a. Weak curvature ridges are present at these locations that we found were not contributing to material spiking and fluid breakaway in the context of flow separation. The oscillatory curvature field and associated ridges correlate directly with the piecewise linear curvature κ_0 of the airfoil surface representation (dashed line) that is inherent to the cubic-spline boundary representation used for the design of the airfoil. The three ridges are hence a geometric artifact and should not be interpreted as significant spiking events.

We can reduce the oscillatory trend from the spline parametrization by filtering the time integral of $\partial_{\eta_{ss}} \hat{v}$ with a kernel width based on the approximate distance between two spline segments. The filtered solution (red line) successfully recovers the underlying correct function and identifies a single spiking point at $x/c = 0.45$ (red circle) upstream of the separation point.

Figure 20b shows the curvature scalar field $\tilde{\kappa}_0^{0.25}$ at t_0 in x and y coordinates, with the ridge highlighted in magenta and the spiking point from Eulerian on-wall quantities in red. With the close match of the backbone-wall intersection at $x/c = 0.46$ and the Eulerian criterion at $x/c = 0.45$, we demonstrate that the spiking point can be extracted from on-wall-based quantities even with approximate parametrization of the boundary, as used in engineering applications.

In Figs. 16 and 17, we show that the global separation of the fluid particles traces back to the formation of an initial material spike at

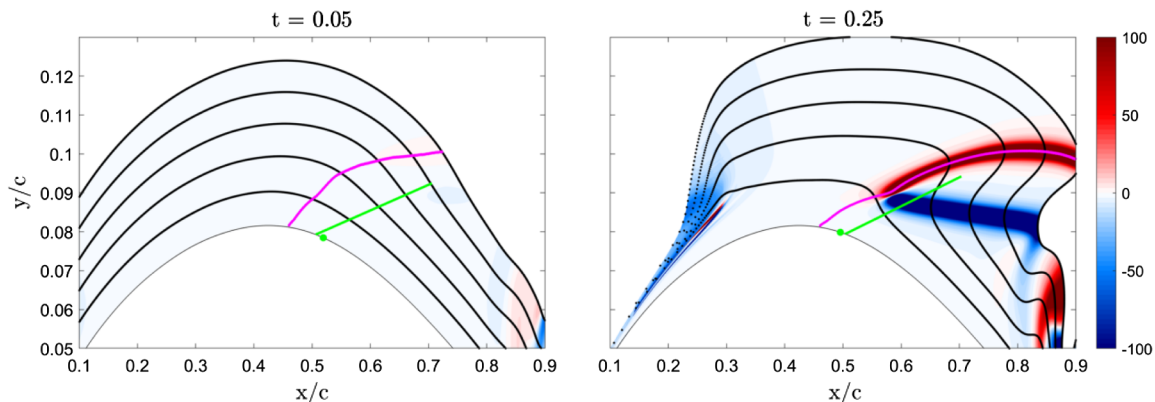


Fig. 17 Advected curvature scalar field with material lines (black) and Lagrangian backbone of separation $\mathcal{B}(t)$ (magenta). Zero-skin-friction point and linear separation line in green. Y axis stretched.

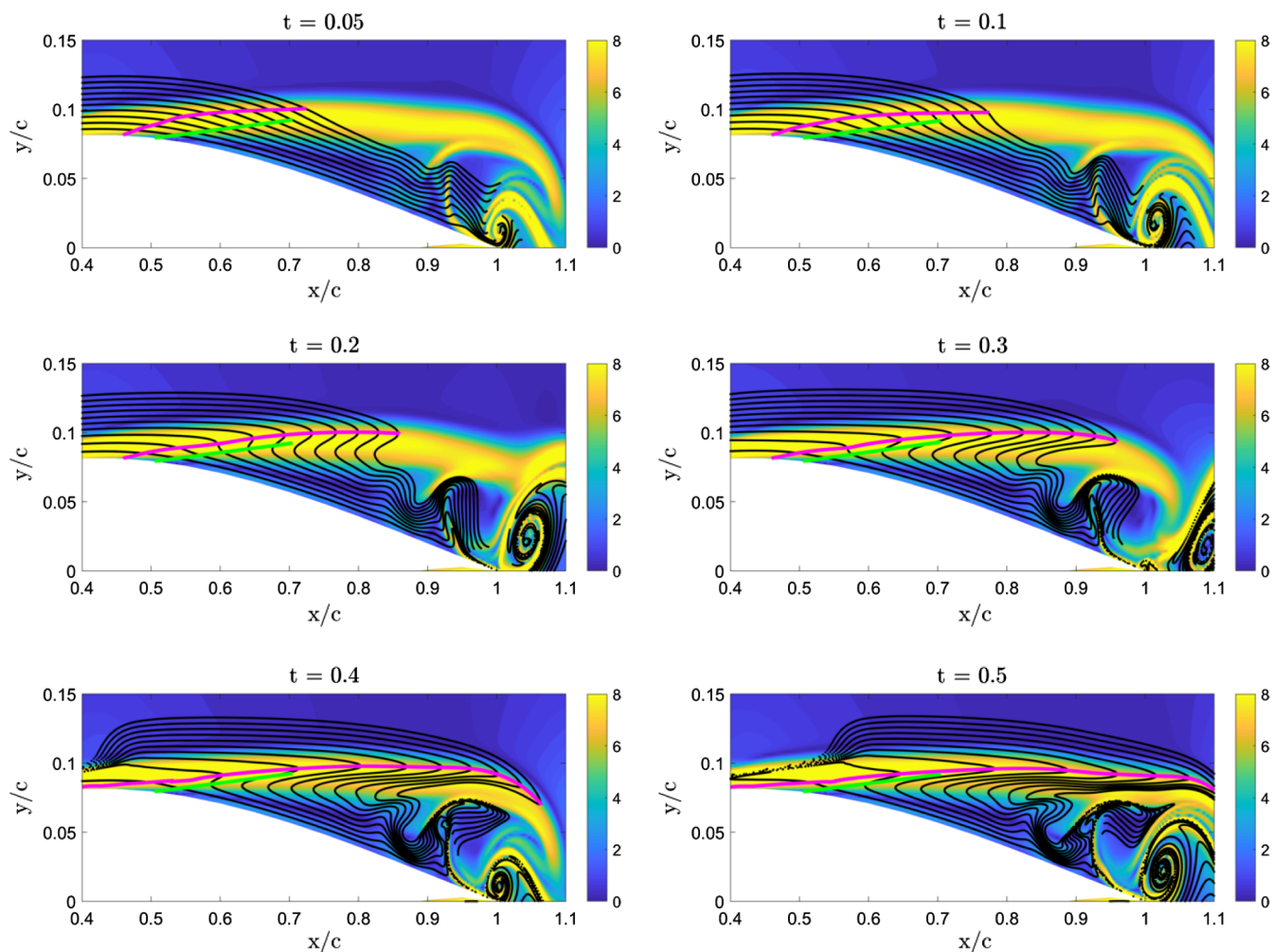


Fig. 18 Backward-time FTLE field (contour plot) computed from t to $t - T$ over $T = 0.36$: advected material lines from zero to t (black), Lagrangian backbone of separation (magenta), and asymptotic separation profile (green). Y axis stretched.

midchord, shortly upstream of the asymptotic separation point. For larger integration time intervals, however, an additional curvature ridge with an origin at the leading edge is detected (see Fig. 17). This sharp spike in the material line occurs only in the vicinity of the wall and has no direct connection to the global separation event at midchord. Of course, when the leading-edge ridge advects to the location of the asymptotic separation manifold, the particles do follow this manifold.

Figure 21 shows the advection of a Lagrangian particle sheet at the leading edge to visualize the Lagrangian flow behavior at the stagnation point in more detail: the local contraction of the streamlines

forces the fluid to accelerate, and the particles closer to the leading edge are initialized on streamlines with higher velocity, leading to upwelling and folding of the material line. The leading edge spike is therefore rather the result of the displacement of streamlines by the growing boundary layer and the associated normal velocity than an event associated with separating flow. We conclude that the leading-edge spike formation is an artifact from the stagnation point flow and is not an indication of flow separation in this case. A more detailed analysis of this phenomenon will be subject to future studies.

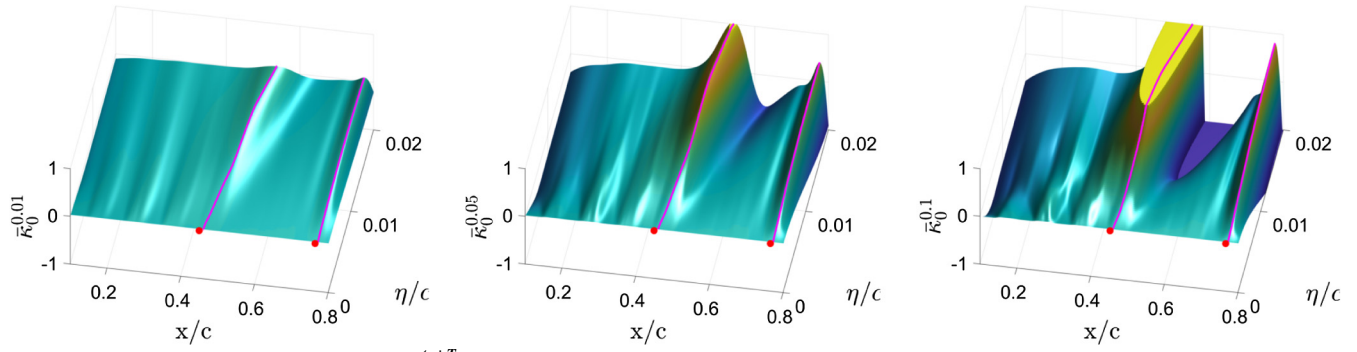


Fig. 19 Surface plot of curvature scalar field $\bar{\kappa}_0^{t_0+T}$ for $T = 0.01, 0.05$, and 0.10 with wall-normal coordinate on y axis: backbone (magenta), and spiking point (red).

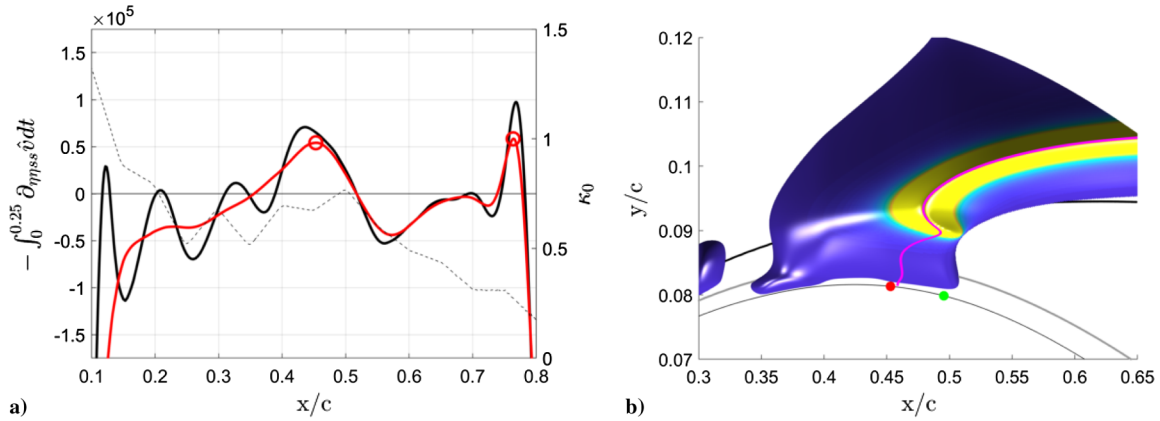


Fig. 20 Representations of a) $-\int_0^{0.25} \partial_{\eta_{ss}} \hat{v} dt$ in black, and b) curvature change field $\log(\bar{\kappa}_0^{0.25})$ at x_0 with backbone (magenta) and Lagrangian spiking point (red) identified from Eulerian on-wall quantities: displacement thickness (black), momentum thickness (gray), and zero-skin-friction point (green).

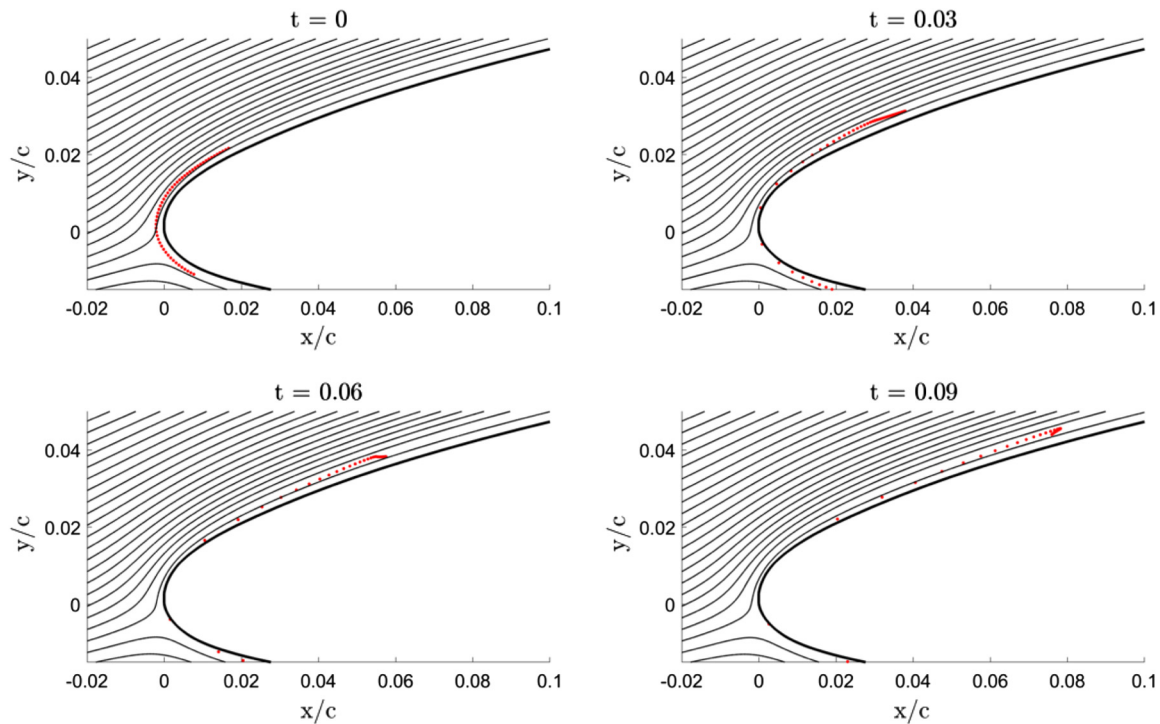


Fig. 21 Advection of a set of particles at the leading edge. Streamlines shown in black.

V. Conclusions

Kinematic aspects of flow separation have been investigated in external aerodynamics by extracting the initial motion of upwelling fluid material from the wall and its relation to the long-term attracting manifolds in the flowfield. Although the wall-bounded kinematics

are governed by the formation of a material spike upstream of the asymptotic separation point and ejection of particles in direction of the separation line, it was shown that the off-wall trajectories of the fluid tracers are driven by attracting ridges in the finite-time Lyapunov exponents. Therefore, the complete pathway of Lagrangian flow

separation was obtained: from the initial upwelling at the spiking point over the ejection of particles along the asymptotic separation profile to the attracting LCSs.

For the flow around a circular cylinder and a cambered NACA 65 (1)-412 airfoil, the footprint of the initial material upwelling, i.e. the spiking point, was determined by evaluating the curvature of Lagrangian fluid tracers and by extracting high-order on-wall derivatives of the normal velocity as proposed in Ref. [12]. An exact match of the Lagrangian and Eulerian criterion for the start of material line spiking verifies the Eulerian criterion and associated the principal location of material upwelling for the first time in two test cases, i.e., the cylinder flow and the flow over an airfoil. For the latter, the spiking point was recovered by appropriately filtering the spurious oscillations in the velocity derivative induced by the spline-based boundary parametrization of the NACA profile, thereby showing that this method is robust to noise. Determining the spiking points requires the extraction of high-order velocity derivatives, which is challenging for general geometries and in experimental settings because it requires very high-resolution data and an accurate representation of the geometry.

With the ability to compute the birth of separation instantaneously from Eulerian on-wall data, the Lagrangian pathway from the spiking point to the asymptotic separation profile can be used as input parameters for dynamic flow controllers. In future work, the aim will be to report on the control of Lagrangian separation, as well as to address the impact of turbulence modeling and the application of the fluid spike extraction in time-averaged flows at high Reynolds numbers.

Acknowledgments

We gratefully acknowledge funding by the U.S. Air Force Office of Scientific Research under FA9550-16-1-0392 of the Flow Control Program and from Solar Turbines. Mattia Serra would like to acknowledge support from the Schmidt Science Fellowship. The provision of subroutines for particle tracking from Paul Fischer of the University of Illinois is greatly appreciated.

References

- [1] Schlichting, H., and Gersten, K., *Boundary-Layer Theory*, Springer-Verlag, Berlin, 2017, p. 293.
- [2] Amitay, M., Smith, B., and Glezer, A., "Aerodynamic Flow Control Using Synthetic Jet Technology," *36th AIAA Aerospace Sciences Meeting and Exhibit*, AIAA Paper 1998-0208, 1998.
- [3] Amitay, M., Smith, D. R., Kibens, V., Parekh, D. E., and Glezer, A., "Aerodynamic Flow Control over an Unconventional Airfoil Using Synthetic Jet Actuators," *AIAA Journal*, Vol. 39, No. 3, 2001, pp. 361–370. <https://doi.org/10.2514/2.1323>
- [4] Glezer, A., and Amitay, M., "Synthetic Jets," *Annual Review of Fluid Mechanics*, Vol. 34, No. 1, 2002, pp. 503–529. <https://doi.org/10.1146/annurev.fluid.34.090501.094913>
- [5] Haller, G., "Exact Theory of Unsteady Separation for Two-Dimensional Flows," *Journal of Fluid Mechanics*, Vol. 512, Aug. 2004, p. 257–311. <https://doi.org/10.1017/S0022112004009929>
- [6] Weldon, M., Peacock, T., Jacobs, G., Helu, M., and Haller, G., "Experimental and Numerical Investigation of the Kinematic Theory of Unsteady Separation," *Journal of Fluid Mechanics*, Vol. 611, Sept. 2008, pp. 1–11. <https://doi.org/10.1017/S0022112008002395>
- [7] Haller, G., "Distinguished Material Surfaces and Coherent Structures in 3D Fluid Flows," *Physica D*, Vol. 149, No. 4, 2001, pp. 248–277. [https://doi.org/10.1016/S0167-2789\(00\)00199-8](https://doi.org/10.1016/S0167-2789(00)00199-8)
- [8] Haller, G., "Finding Finite-Time Invariant Manifolds in Two-Dimensional Velocity Fields," *Chaos*, Vol. 10, No. 1, 2000, p. 99–108. <https://doi.org/10.1063/1.166479>
- [9] Haller, G., "Lagrangian Coherent Structures from Approximate Velocity Data," *Physics of Fluids*, Vol. 14, No. 6, 2002, pp. 1851–1861. <https://doi.org/10.1063/1.1477449>
- [10] Haller, G., "A Variational Theory of Hyperbolic Lagrangian Coherent Structures," *Physica D*, Vol. 240, No. 7, 2011, pp. 574–598. <https://doi.org/10.1016/j.physd.2010.11.010>
- [11] Shadden, S. C., Lekien, F., and Marsden, J. E., "Definition and Properties of Lagrangian Coherent Structures from Finite-Time Lyapunov Exponents in Two-Dimensional Aperiodic Flows," *Physica D*, Vol. 212, Nos. 3–4, 2005, pp. 271–304. <https://doi.org/10.1016/j.physd.2005.10.007>
- [12] Serra, M., Vetel, J., and Haller, G., "Exact Theory of Material Spike Formation in Flow Separation," *Journal of Fluids Mechanics*, Vol. 845, June 2018, pp. 51–92. <https://doi.org/10.1017/jfm.2018.206>
- [13] Serra, M., Crouzat, S., Simon, G., Vétel, J., and Haller, G., "Material Spike Formation in Highly Unsteady Separated Flows," *Journal of Fluid Mechanics*, Vol. 883, Jan. 2020, Paper A30. <https://doi.org/10.1017/jfm.2019.876>
- [14] Kopriva, D. A., *Implementing Spectral Methods for Partial Differential Equations*, Springer, New York, 2009, p. 134.
- [15] Gassner, G. J., Winters, A. R., and Kopriva, D. A., "Split Form Nodal Discontinuous Galerkin Schemes with Summation-by-Parts Property for the Compressible Euler Equations," *Journal of Computational Physics*, Vol. 327, Dec. 2016, pp. 39–66. <https://doi.org/10.1016/j.jcp.2016.09.013>
- [16] Klose, B. F., Jacobs, G. B., and Kopriva, D. A., "On the Robustness and Accuracy of Marginally Resolved Discontinuous Galerkin Schemes for Two Dimensional Navier–Stokes Flows," *AIAA Scitech 2019 Forum*, AIAA Paper 2019-0780, 2019.
- [17] Nelson, D. A., and Jacobs, G. B., "DG-FTLE: Lagrangian Coherent Structures with High-Order Discontinuous-Galerkin Methods," *Journal of Computational Physics*, Vol. 295, Aug. 2015, pp. 65–86. <https://doi.org/10.1016/j.jcp.2015.03.040>
- [18] Mohseni, K., Lipinski, D., and Cardwell, B., "A Lagrangian Analysis of a Two-Dimensional Airfoil with Vortex Shedding," *Journal of Physics, A: Mathematical and Theoretical*, Vol. 41, No. 34, 2008, pp. 1–22.
- [19] Kopriva, D. A., "A Staggered-Grid Multidomain Spectral Method for the Compressible Navier–Stokes Equations," *Journal of Computational Physics*, Vol. 143, No. 1, 1998, pp. 125–158. <https://doi.org/10.1006/jcph.1998.5956>
- [20] Jacobs, G. B., Kopriva, D. A., and Mashayek, F., "A Comparison of Outflow Boundary Conditions for the Multidomain Staggered-Grid Spectral Method," *Numerical Heat Transfer, Part B: Fundamentals*, Vol. 44, No. 3, 2003, pp. 225–251. <https://doi.org/10.1080/713836380>
- [21] Nelson, D. A., Jacobs, G. B., and Kopriva, D. A., "Effect of Boundary Representation on Viscous, Separated Flows in a Discontinuous-Galerkin Navier–Stokes Solver," *Theoretical Computational Fluid Dynamics*, Vol. 30, No. 4, 2016, pp. 363–385. <https://doi.org/10.1007/s00162-016-0388-7>
- [22] Mittal, K., Dutta, S., and Fischer, P., "Nonconforming Schwarz-Spectral Element Methods for Incompressible Flow," *Computers and Fluids*, Vol. 191, Sept. 2019, Paper 104237. <https://doi.org/10.1016/j.compfluid.2019.104237>
- [23] Williamson, C., "Vortex Dynamics in the Cylinder Wake," *Annual Review of Fluid Mechanics*, Vol. 28, No. 1, 1996, pp. 477–539. <https://doi.org/10.1146/annurev.fl.28.010196.002401>
- [24] Rockwood, M. P., and Green, M. A., "Real-Time Identification of Vortex Shedding in the Wake of a Circular Cylinder," *AIAA Journal*, Vol. 57, No. 1, 2019, pp. 223–238. <https://doi.org/10.2514/1.J057383>
- [25] Kamphuis, M., Jacobs, G. B., Chen, K., Spedding, G., and Hoeijmakers, H., "Pulse Actuation and Its Effects on Separated Lagrangian Coherent Structures for Flow over a Cambered Airfoil," *2018 AIAA Aerospace Sciences Meeting*, AIAA Paper 2018-2255, 2018.

N. D. Sandham
Associate Editor